Linear and nonlinear interactions between an interface and bulk vortices in Richtmyer–Meshkov instability

Chihiro Matsuoka, Katsunobu Nishihara, Francisco Cobos-Campos

Physics of Plasmas ARTICLE scitation.org/journal/php

Linear and nonlinear interactions between an interface and bulk vortices in Richtmyer–Meshkov instability

Cite as: Phys. Plasmas **27**, 112301 (2020); doi: 10.1063/5.0016553
Submitted: 5 June 2020 · Accepted: 17 August 2020 ·
Published Online: 2 November 2020

Chihiro Matsuoka,[1,a)] Katsunobu Nishihara,[2,b)] and Francisco Cobos-Campos[3,c)]

AFFILIATIONS

[1]Laboratory of Applied Mathemetics, Graduate School of Engineering, Osaka City University, Sugimoto, Sumiyoshi, Osaka 558-8585, Japan
[2]Institute of Laser Engineering, Osaka University, Suita, Osaka 565-0871, Japan
[3]Instituto de Investigaciones Energéticas y Aplicaciones Industriales (INEI), Universidad de Castilla-La Mancha, Ciudad Real, 13071, Spain

Note: This paper is part of the Special Collection: Non-Equilibrium Dynamics, Interfaces and Mixing in Plasmas.
[a)]**Author to whom correspondence should be addressed:** cmatsuoka@osaka-cu.ac.jp. **Present address:** Nambu Yoichiro Institute of Theoretical and Experimental Physics (NITEP), Osaka City University, Osaka City University Advanced Mathematical Institute (OCAMI), Sugimoto, Sumiyoshi, Osaka 558-0022, Japan.
[b)]**Present address:** Graduate School of Engineering, Osaka City University, Sugimoto, Sumiyoshi, Osaka 558-8585, Japan.
[c)]**Present address:** Fluid Mechanics Group, UC3M, Madrid, Spain.

ABSTRACT

When a planar shock hits a corrugated interface between two fluids, the Richtmyer–Meshkov instability (RMI) occurs. Vortices are generated in bulk behind the transmitted and reflected shocks in RMI. As the shock intensity becomes larger, the stronger bulk vortices are created. The nonlinear evolution of RMI is investigated within the vortex sheet model (VSM), taking the nonlinear interaction between the interface and the vortices into account. The fluid becomes incompressible as the shocks move away from the interface, and VSM can then be applied. The vorticity and position of the bulk vortices obtained from the compressible linear theory [F. Cobos-Campos and J. G. Wouchuk, Phys. Rev. **E93**, 053111 (2016)] are applied as initial conditions of the bulk point vortices in VSM. The suppression of RMI due to the bulk vortices is observed in the region such that the corrugation amplitude is less than one-tenth of the wavelength, and the reduction of the growth is quantitatively evaluated and compared with the compressible linear theory. In the nonlinear stage, the interaction between the interface and the bulk vortices strongly affects the interfacial shape and the dynamics of bulk vortices, e.g., the creation of a vortex pair is observed. Strong bulk vortices behind the transmitted shock enhance the growth of spike, supplying flow from spike root to its top and mushroom umbrella in the fully nonlinear stage.

I. INTRODUCTION

The Richtmyer–Meshkov instability (RMI)[1–4] is a shock-induced inviscid fluid instability with density stratification, which leads to non-uniform and non-equilibrium turbulence. RMI is important in various areas such as astrophysical supernova explosion,[5–9] supersonic combustion, inertial confinement fusion (ICF),[10–12] and atmospheric and planetary sciences. When a shock wave crosses the interface in RMI, the transmitted shock and the reflected shock or rarefaction wave occur at the interfaces. Here, we consider the case of the reflected shock. Non-uniform velocity shears are induced at the interface, and the transmitted and reflected shocks involve ripples due to the passage of a shock wave across a corrugated interface in RMI.[3,13–17] Owing to the conservation of tangential velocity at the rippled shock fronts, transverse velocity perturbations are generated inside the compressed fluids, which leads to the vorticity generation in the bulk.[14,16,18–24]

Immediately after the shocks pass through the corrugated interface, the compressibility is dominant, where if the amplitude of the interface is sufficiently small, the compressible linear theory is valid.[14,25] Cobos-Campos and Wouchuk theoretically calculated and visualized the magnitude of the vorticities of bulk vortices generated

by the shocks. They also concluded that the bulk vortices suppress the growth of the interface in RMI within the linear theory,[24,26] as has been known in previous works.[14,18] In their linear theory, the positions and the strengths of bulk vortices can be determined from the pre-shock Atwood number, adiabatic exponent of the fluids, and the shock intensity with the asymptotic linear growth velocity of the interface. Cobos-Campos and Wouchuk also confirmed that their analytical calculations fit well with real experiments of RMI.[24]

When the shocks go away from the corrugated interface, we can treat the system as incompressible and the non-uniform velocity shear as a non-uniform vortex sheet.[15] By the Lagrange's theorems on vorticity,[27] the vorticity generated in the bulk does not disappear in the perfect fluid; therefore, the bulk vortices interact with the vortex sheet, which provides a different evolution from RMI without bulk vortices. In the current study, approximating the bulk vortices by point vortices, we investigate the nonlinear interaction between the bulk vortices and the interface using the vortex sheet model (VSM).[28–31]

VSM is a powerful tool for investigating the nonlinear interfacial dynamics such as the Kelvin–Helmholtz instability,[32,33] the Rayleigh–Taylor instability,[28,34–36] and RMI,[9,28–31,37,38] in which the unstable interface is regarded as a vortex sheet without thickness.[39] In VSM, the interfacial velocity is provided as the vortex-induced velocity by the Birkhoff–Rott equation.[39–42] By controlling the regularized parameter δ in the Birkhoff–Rott equation,[33] VSM can provide the long-time behavior of an unstable interface. When we select $\delta \neq 0$, which is called the vortex method,[39] we can calculate the roll-up of the interface. On the other hand, when we select the regularized parameter $\delta = 0$, the numerical results by VSM become spectrally accurate,[43] which enables us to compare the numerical results with the analytical calculations.[28,30,44] In the calculation of $\delta = 0$, Moore's curvature singularity occurs,[28,43,45] and the numerical calculation breaks down before the roll-up of the interface appears. We adopt both calculations of $\delta = 0$ and $\delta \neq 0$ in the present study.

The compressible linear theory[14,18,24] shows that the linear growth rate consists of two terms. One is due to the non-uniform velocity shear deposited on the interface when the planar shock passes through the corrugated interface. The other is the term caused by the bulk vortices formed by the rippled transmission and reflection shocks. In the present work, a non-uniform velocity shear is given as an initial condition in VSM, and the bulk vortices are approximated by point vortices. The vorticity of bulk point vortices and their initial distances from the interface are given by the values obtained from the linear theory.[24] The nonlinear dynamics of the system due to their nonlinear interaction are numerically calculated and compared with the cases without the point vortices. Numerical results show that the bulk vortices have opposing effects on the instability growth dynamics. In the earlier stage such that the corrugation amplitude is less than 1/10 of the wavelength, the bulk vortices suppress the RMI growth corresponding to the initial velocity shear at the interface, while the strong bulk vortices enhance the growth of spike supplying flow from spike root to its top and mushroom umbrella in the fully nonlinear stage.

This paper is organized as follows. In Sec. II, we briefly describe the linear growth rate of RMI derived from the compressible linear theory, which is used to normalize all physical quantities and to determine the initial conditions of bulk point vortices in the current study. In Sec. III, we provide an overview of the mathematical model for VSM with bulk point vortices and derive the governing equations for describing the motion of the unstable interface coexisting bulk point vortices. In Sec. IV, we present the numerical results for both cases of the regularized parameter $\delta = 0$ and $\delta \neq 0$, in which the initial conditions for VSM are determined from the compressible linear theory, and the calculations for $\delta = 0$ are compared with the analytical results by the linear theory. In this section, we show that the existence of bulk vortices suppresses RMI in the early stage, while the bulk vortices enhance the spike growth in the fully nonlinear stage of RMI. Section V is devoted to conclusion.

II. OVERVIEW OF THE LINEAR GROWTH RATE IN RMI

RMI develops when a plane shock collides with a corrugated interface separating two different fluids. In this work, we only consider the case in which a shock is reflected. Once the transmitted and reflected shock fronts have been formed and have started to separate from the contact surface at $t = +0$, the initial corrugation of the interface begins to grow, and the shock fronts are deformed. As they move into the fluid, they leave density and vorticity perturbation behind them.[14,18,46–48] The interface perturbation shows damped oscillations, and when the shock fronts go away from the interface more than a wavelength of the perturbation,[3] the perturbed contact surface reaches a constant velocity, which we call the asymptotic linear growth rate.[14,18,24,46,48,49]

The asymptotic linear growth rate can be exactly expressed in the following form:[14,18,24]

$$v_{lin^c} = \frac{\rho_2 \delta v_2^* - \rho_1 \delta v_1^*}{\rho_1 + \rho_2} - \frac{\rho_2 F_2 - \rho_1 F_1}{\rho_1 + \rho_2} = v_{lin} - \frac{\rho_2 F_2 - \rho_1 F_1}{\rho_1 + \rho_2}, \tag{1}$$

where v_{lin} is given by

$$v_{lin} = \frac{\rho_2 \delta v_2^* - \rho_1 \delta v_1^*}{\rho_1 + \rho_2}. \tag{2}$$

Equation (2) is derived from the deposition of vorticity at the interface at $t = +0$, and it depends only on the initial tangential velocities, δv_1^* and δv_2^*, of generated at both sides of the interface just after the incident shock passes through it ($t = +0$), whose expression can be found in Refs. 1, 3, and 25, and also refer to Eq. (16) in Ref. 24. Here, the suffixes 1 and 2 denote the heavy and light fluids, and the transmitted and reflected shocks propagate in region 1 (heavy) and region 2 (light), respectively. The mass density is the post-shock density. A completely analytical model to solve the zero-order profiles when a shock is reflected has been recently published.[17] The term v_{lin} is enough to estimate the asymptotic growth velocity for weak shocks.[14] Hereafter, we call v_{lin} in Eq. (2) simply as the linear growth rate.

The terms F_1 and F_2 in Eq. (1) represent the sonic interaction between the rippled shock fronts and the rippled contact surface for $t > 0+$. They can be written as integrals of the pressure perturbations along the shock front trajectories[14,18,48] (we can also regard F_1 and F_2 as averaged measures of the vorticity field left by the rippled shock fronts[14]). The second term in Eq. (1) comes from the vorticity generation by the deformed shock fronts in the bulk fluid. Their calculation requires iterating on a system of coupled functional equations.[18,24] It should also be noted that the second term in Eq. (1) generally reduced the linear growth v_{lin}.

The linear growth velocity v_{lin} in Eq. (2) plays an important role in normalizing physical quantities in the current study as the initial velocity shear of the interface. We consider here an interface that has initially sinusoidal velocity shear with the maximum value of the difference of tangential velocity between the heavy and light fluids, $2v_{lin}$ with the wavenumber k. In calculations by VSM, the length and time are normalized by the wavenumber k and the initial shear velocity v_{lin} such as kx, ky, and $kv_{lin}t$. The linear growth rate is also used for the normalization of the strengths of point vortices in $\boldsymbol{W}_p$ [refer to Eq. (5)] and bulk vorticity ω_i [$i = 1, 2$, refer to Eq. (7) and Table I] below.

III. GOVERNING EQUATIONS FOR THE VORTEX SHEET MODEL WITH BULK POINT VORTICES

In this section, we provide an overview of the mathematical model for VSM with bulk point vortices. A more detailed explanation is also found in Ref. 31. In applying VSM, the bulk vortices are approximated by bulk point vortices. We consider the state that the shocks have traveled a distance greater than a wavelength. Then the system can be regarded as incompressible and irrotational except the interface (contact surface) and bulk point vortices. We assume that the interface does not have the thickness, and the point vortices are sizeless singular points in the bulk.[27,50] We consider the two-dimensional flow in which a fluid interface with density and tangential velocity jumps across that exists. Since the system is described by the potential flow, the Laplace equation $\Delta\phi_i$ ($i = 1, 2$) holds in each fluid region across the interface, where ϕ_i is the velocity potential in fluid i.

Now we parameterize points on the interface $\boldsymbol{x} = \boldsymbol{X}$ as

$$\boldsymbol{X}(e,t) = [X(e,t), Y(e,t)]$$

using a Lagrangian parameter e ($-\pi \le e \le \pi$). We assume the periodicity in the x direction. When bulk vortices exist in the system, the vortex induced fluid velocity $\boldsymbol{W}$ at an arbitrary point $\boldsymbol{x} = (x, y)$ is given as the sum of the two velocities

$$\boldsymbol{W} = \boldsymbol{W}_s + \boldsymbol{W}_p, \tag{3}$$

in which $\boldsymbol{W}_s = (W_{s,x}, W_{s,y})$ is the velocity by the contribution from the interface

$$W_{s,x}(x,y) = -\frac{1}{4\pi}\int_{-\pi}^{\pi} \frac{\gamma(e',t)s_e(e',t)\sinh(y - Y(e',t))}{\cosh(y - Y(e',t)) - \cos(x - X(e',t)) + \delta^2}de',$$
$$W_{s,y}(x,y) = \frac{1}{4\pi}\int_{-\pi}^{\pi} \frac{\gamma(e',t)s_e(e',t)\sin(x - X(e',t))}{\cosh(y - Y(e',t)) - \cos(x - X(e',t)) + \delta^2}de', \tag{4}$$

where $\boldsymbol{\gamma} = \boldsymbol{u}_2 - \boldsymbol{u}_1$, and $\gamma = \boldsymbol{\gamma}\cdot\boldsymbol{t} = \partial\Gamma/\partial s$ denotes the (true) vortex sheet strength derived from the circulation $\Gamma \equiv \phi_2 - \phi_1$, in which the velocity potential ϕ_i ($i = 1, 2$) is related to the fluid velocity $\boldsymbol{u}_i$ as $\boldsymbol{u}_i = \nabla\phi_i$, and s is the arc length, and $\boldsymbol{t}$ is the unit tangential vector of the interface, respectively. Here, the subscript e denotes the differentiation with respect to e and $s_e = \sqrt{X_e^2 + Y_e^2}$. We take the principal value of the integral (4) when the point (x, y) is on the interface: $(x, y) = (X, Y)$. Equation (4) corresponds to the Birkhoff–Rott equation[40–42] if (x, y) is on the interface. The regularized parameter δ[33] in Eq. (4) is set to $\delta = 0$ when we compare the numerical results by VSM with the analytical results (refer to Sec. IV C).

On the other hand, $\boldsymbol{W}_p = (W_{p,x}, W_{p,y})$ in (3) is the velocity by the contribution from bulk vortices

$$W_{p,x}(x,y) = -\frac{1}{4\pi}\sum_{j=1}^{N_p} \frac{\gamma_{p,j}\sinh(y - y_{p,j}(t))}{\cosh(y - y_{p,j}(t)) - \cos(x - x_{p,j}(t)) + \delta^2},$$
$$W_{p,y}(x,y) = \frac{1}{4\pi}\sum_{j=1}^{N_p} \frac{\gamma_{p,j}\sin(x - x_{p,j}(t))}{\cosh(y - y_{p,j}(t)) - \cos(x - x_{p,j}(t)) + \delta^2}, \tag{5}$$

where N_p is the number of point vortices and $\gamma_{p,j}$ denotes the strength of point vortex j ($j = 1, 2, \ldots N_p$).

Here, we mention the relation between the strength γ or $\gamma_{p,j}$ ($j = 1, 2, \ldots, N_p$) and the vorticity of the system $\boldsymbol{\omega} = \nabla\times\boldsymbol{u}$, where $\boldsymbol{\omega} = \omega\hat{\boldsymbol{e}}_z$, $\hat{\boldsymbol{e}}_z$—the unit vector in the z direction. We can also define the strength γ (or $\gamma_{p,j}$) using the integral as

$$\gamma = \oint \omega ds,$$

where ds is the line element along the interface or the streamline encircling ω. Dividing γ by the linear growth rate v_{lin} in Eq. (2), we have

$$\frac{\gamma}{v_{lin}} = \frac{\oint\omega ds}{v_{lin}} = \oint\frac{\omega}{v_{lin}}ds = k\oint\frac{\omega}{kv_{lin}}ds. \tag{6}$$

For the vortex sheet or point vortices, the distribution ω has δ-functional form.[27,42,50] Taking this into account and performing the line integral in Eq. (6) over a wavelength, we obtain the $\gamma - \omega$ correspondence

$$\frac{\gamma}{v_{lin}} = \frac{\omega}{kv_{lin}}, \tag{7}$$

from which we can regard the dimensionless vorticity $\omega/(kv_{lin})$ as the dimensionless vortex sheet strength γ or the dimensionless point vortex strength $\gamma_{p,j}$ normalized by the linear growth rate v_{lin}. We use the relation (7) in determining the initial conditions for the nonlinear calculations by VSM (refer to Table I in Sec. IV A).

In VSM, we define the interfacial velocity $\boldsymbol{u}^+$ of a Lagrangian point labeled by e as

$$\boldsymbol{u}^+(e,t) = \boldsymbol{W}|_{\boldsymbol{x}=\boldsymbol{X}} + \frac{\tilde{\alpha}\gamma}{2}\boldsymbol{t}, \tag{8}$$

TABLE I. Initial conditions for the calculations by VSM derived from the linear theory. The vorticity $\omega_i/(kv_{lin})$ ($i = 1, 2$) is defined at $kx = \pi/2$.

$(p_1 - p_0)/p_1$	$\omega_1/(kv_{lin})$	ky_1	$\omega_2/(kv_{lin})$	ky_2	v_{lin}^c/v_{lin}	A
0.5	0.175928	−2.063134	0.026188	6.398230	0.947413	0.307182
0.7	0.390033	−1.480230	0.049665	4.828697	0.876893	0.277927
0.8	0.600444	−1.254237	0.066041	4.184017	0.821151	0.244675
0.9	1.071423	−1.019868	0.087859	3.560310	0.745436	0.165796

where $\boldsymbol{W}|_{\boldsymbol{x}=\boldsymbol{X}} \equiv (U, V)$ corresponds to the average velocity $(\boldsymbol{u}_1 + \boldsymbol{u}_2)/2$ at the interface and $\tilde{\alpha}$ is an artificial parameter[28,51] depending on the Atwood number A defined by

$$A = \frac{\rho_1 - \rho_2}{\rho_1 + \rho_2}, \tag{9}$$

in which ρ_i $(i = 1, 2)$ is the post-shock density of fluid i as used in Eqs. (1) and (2). The parameter $\tilde{\alpha}$ controls the magnitude of the tangential velocity. When the regularized parameter $\delta = 0$, we select $\tilde{\alpha}$ as $\tilde{\alpha} = -A$,[28] for which the interfacial velocity $\boldsymbol{u}^+$ becomes a weighted average of two fluids

$$\boldsymbol{u}^+ = \frac{\rho_1 \boldsymbol{u}_1 + \rho_2 \boldsymbol{u}_2}{\rho_1 + \rho_2}, \tag{10}$$

while we select $\tilde{\alpha}$ as $\tilde{\alpha} = -A^2$ when $\delta \neq 0$[28,31] throughout this paper, by which we can suppress the rapid increase in the tangential velocity in rolling-up of the vortex sheet at the late stage.[52]

Equating $\boldsymbol{u}^+$ with the evolution of the interface, we have the interfacial velocity for the Lagrangian motion as

$$\frac{\mathrm{d}\boldsymbol{X}}{\mathrm{d}t} = \boldsymbol{W}|_{\boldsymbol{x}=\boldsymbol{X}} + \frac{\tilde{\alpha}\gamma}{2}\boldsymbol{t}, \tag{11}$$

where

$$\frac{\mathrm{d}}{\mathrm{d}t} = \frac{\partial}{\partial t} + \boldsymbol{u}^+ \cdot \nabla$$

is the Lagrangian derivative in the frame moving with the interface.

A point vortex velocity is given by substituting its location $\boldsymbol{x} = \boldsymbol{x}_{p,i}$ into (3)

$$\frac{\mathrm{d}\boldsymbol{x}_{p,i}}{\mathrm{d}t} = \boldsymbol{W}_s|_{\boldsymbol{x}=\boldsymbol{x}_{p,i}} + \boldsymbol{W}_p|_{\boldsymbol{x}=\boldsymbol{x}_{p,i}} \quad (i = 1, 2, \ldots, N_p), \tag{12}$$

where the term of $j = i$ (own contribution) in the integral (5) is excluded from the summation.

Differentiating the Bernoulli equation obtained from the Euler equation with respect to e,[15,28,31] we obtain the evolution equation for the vortex sheet strength γ as follows:

$$\frac{\mathrm{d}\gamma}{\mathrm{d}t} = \frac{2A}{s_e}\left(X_e\frac{\mathrm{d}U}{\mathrm{d}t} + Y_e\frac{\mathrm{d}V}{\mathrm{d}t}\right) - \frac{(1+\tilde{\alpha}A)\gamma}{s_e^2}(X_eU_e + Y_eV_e) + \frac{A+\tilde{\alpha}}{4s_e}(\gamma^2)_e. \tag{13}$$

Solving Eqs. (11), (12), and (13) simultaneously by taking the integrals (4) and (5) into account, we can determine the motion of the interface and the trajectories of bulk point vortices.

IV. NUMERICAL RESULTS

In this section, we present the nonlinear evolution of the unstable interface by VSM. In order to relate the incompressible nonlinear calculations to the compressible RMI continuously, we adopt the analytical results derived from the compressible linear theory[14,17,18,24–26,53,54] as the initial conditions for the calculations by VSM.

A. Initial conditions for bulk point vortices derived from the linear theory

In this subsection, we briefly mention the physical quantities obtained by the linear analysis, in which the bulk vortices spread with finite vorticities. We adopt the centers of these vorticities as point vortices in calculations by VSM. Table I shows the physical quantities derived from the compressible linear theory,[24] which correspond to the initial conditions for bulk point vortices adopted in the calculations by VSM. In Table I, the data were calculated with the same initial pre-shock parameters as in Fig. 3 of Ref. 24; namely, the pre-shock Atwood number is 1/3, and the adiabatic exponents $\gamma_1 = 1.118228$ and $\gamma_2 = 1.1$, respectively. The details of the derivation were written in the reference.

The first row of the table, $(p_1 - p_0)/p_1$, denotes the incident shock intensity, where p_0 and p_1 are the pressure ahead and behind the incident shock.[14,25] From now on, we define the case of $(p_1 - p_0)/p_1 = 0.9$ as case (I). Since we consider inviscid flow, the vorticity stored at any point in bulk is equal to the vorticity generated by the corrugated shock at the instant of time when the wavefront arrived at that point in bulk. The vorticity is generated as a consequence of the conservation of tangential velocity across the rippled shock wave. Cobos-Campos and Wouchuk showed that a maximum or minimum of the perturbed pressure behind the shocks corresponds to the center of a vortex in bulk.[24] In fact, the first zero of the spatial derivative of the pressure perturbation gives the center of the nearest points to the interface, ky_1 and ky_2, and strong vorticities ω_1 and ω_2. These vorticities appear as vortex pairs, and their x coordinates are fixed at $kx = \pm\pi/2$. Their values in Table I (the second and fourth rows) were obtained numerically by the first root of the derivative of Eq. (22) and evaluated the corresponding vorticity expression, Eq. (B3) in Ref. 24. They are normalized by the wavelength and kv_{lin}. The fifth row v_{lin}^c/v_{lin} namely, the ratio of the asymptotic linear growth rate with the bulk vorticity and the linear growth rate without bulk vorticity, is the ratio between the velocities (1) and (2) derived analytically from the linear theory. The Atwood number A in the sixth row is defined using the post-shock density at the interface, which is given by Eq. (9) in the current study. A completely analytical model to solve the zero order profiles when a shock is reflected has been recently published.[17]

The bulk vortices obtained by the linear theory form vortex pairs such that their vorticities become weaker as they are distant from the interface.[24] The normalized vorticities $\omega_1/(kv_{lin})$ and $\omega_2/(kv_{lin})$ in Table I denote the largest vorticities that appear at $kx = \pi/2$ in the heavier fluid (region 1) and the lighter fluid (region 2), respectively. The same vorticities in their magnitude with negative sign appear at $kx = -\pi/2$ and the same y coordinates ky_1 [for $\omega_1/(kv_{lin})$] and ky_2 [for $\omega_2/(kv_{lin})$] in Table I to form vortex pairs. We only consider these four vortices (two vortex pairs) because the vorticities in far distance from the interface rapidly decrease,[24] and we can ignore the effect of them on the interface.

Figure 1 depicts the relation between the distance from the bulk vorticity $|ky_1|$ (black closed circles) and the normalized vorticity in the heavier fluid (region 1) $\omega_1/(kv_{lin})$ (closed squares) as a function of shock intensity $(p_1 - p_0)/p_1$. We see that as the shock intensity increases, the stronger bulk vorticity appears closer to the interface. This tendency is found in the lighter fluid (region 2) as well (refer to Table I). It should be noted that the decrease in the distance $|ky_1|$ is almost linear but the increase in $\omega_1/(kv_{lin})$ is exponential.

B. Initial condition for the interface and numerical methods

As described in Sec. II, all physical quantities are normalized by the wavenumber k and the linear growth rate v_{lin} in Eq. (2), so that

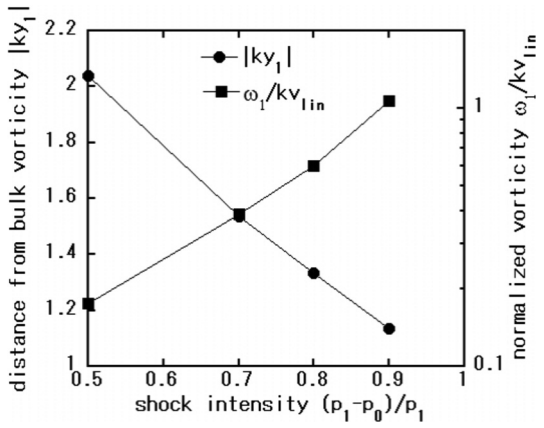

FIG. 1. Relation between the distance from the bulk vorticity $|ky_1|$ and normalized vorticity $\omega_1/(kv_{lin})$.

they are dimensionless. From now on, the dimensionless variables space $k\boldsymbol{x}$, time $kv_{lin}t$, vortex sheet strength γ/v_{lin}, and strength of point vortex $\gamma_{p,j}/v_{lin}$ $(j = 1, 2, 3, 4)$ are used as $\boldsymbol{x}$, t, γ, and $\gamma_{p,j}$ $(j = 1, 2, 3, 4)$. Under the above normalizations, the initial condition for the interface is given as

$$\begin{aligned} x(e,0) &= e, \quad (-\pi \le e \le \pi) \\ y(e,0) &= 0, \\ \gamma(e,0) &= -2\sin e, \end{aligned} \tag{14}$$

for both cases of the regularized parameter $\delta = 0$ and $\delta \neq 0$. As shown in Eq. (14), the initial perturbation exists only on the vortex sheet strength γ, and there is no corrugation on the initial interface.

As described in Sec. IV A, we regard the initial position of point vortices as the center of bulk vorticities in the linear theory. Further, taking the $\gamma - \omega$ correspondence Eq. (7) into account, we set the initial condition of four point vortices P_i $(i = 1, 2, 3, 4)$ [two vortex pairs, $(\mathrm{P}_1, \mathrm{P}_3)$ and $(\mathrm{P}_2, \mathrm{P}_4)$] to compare VSM to the linear theory described in Secs. II and IV A as

$$\begin{aligned} \mathrm{P}_1 &: x_{p,1}(0) = \frac{\pi}{2},\ y_{p,1}(0) = y_2,\ \gamma_{p,1} = \omega_2/k, \\ \mathrm{P}_2 &: x_{p,2}(0) = \frac{\pi}{2},\ y_{p,2}(0) = y_1,\ \gamma_{p,2} = \omega_1/k, \\ \mathrm{P}_3 &: x_{p,3}(0) = -\frac{\pi}{2},\ y_{p,3}(0) = y_2,\ \gamma_{p,3} = -\omega_2/k, \\ \mathrm{P}_4 &: x_{p,4}(0) = -\frac{\pi}{2},\ y_{p,4}(0) = y_1,\ \gamma_{p,4} = -\omega_1/k, \end{aligned} \tag{15}$$

where y_i and ω_i/k $(i = 1, 2)$ are the quantities given in Table I as ky_i and $\omega_i/(kv_{lin})$. We mention that the strength of point vortices $\gamma_{p,i}$ $(i = 1, 2, 3, 4)$ is unchanged with respect to time t from the definition of point vortices.[27,50]

Here, we briefly mention the numerical methods adopted in the current study. When the regularized parameter $\delta = 0$, we adopt the alternate point quadrature method[28,55] for spatial integration of Eq. (4). This scheme is known to be the spectral accuracy.[43] When $\delta \neq 0$, we adopt the conventional trapezoidal rule for spatial integration. For the temporal integration, we use the fourth-order Runge–Kutta scheme throughout this paper for both calculations of $\delta = 0$ and $\delta \neq 0$. The Fredholm equation of the second kind Eq. (13) is solved by iteration with tolerance level 10^{-12}. In order to cut the irregular motion due to the round-off error, we use the filtering technique introduced by Krasny.[33]

When $\delta \neq 0$, we adopt the grid redistribution method using the Newton's method to avoid clustering of grid points.[9,28,56] There is another numerical method to avoid the clustering, which is known as the point insertion scheme.[31,33,35] This method can capture the complicated structure of the vortex sheet at the late stage by inserting grid points successively; however, the roll-up of the vortex sheet is too strong, and the asymptotic growth rate of bubble and spike deviates[35] from the value obtained by the theoretical prediction.[57,58] In addition to that, the point insertion scheme is unsuitable for the calculation of high Atwood numbers. For more details on the numerical schemes adopted here, refer to Refs. 9 and 28.

C. Nonlinear interfacial dynamics by VSM for $\delta = 0$

In this subsection, we present the numerical results by VSM for $\delta = 0$ and compare that with the compressible linear theory. In numerical calculations, the number of grid points N taken on the interface is selected as $N = 1024$ for the calculation of $\delta = 0$. We set the normalized time step Δt as $\Delta t = 10^{-4}$ throughout the calculations for $\delta = 0$.

Figure 2(a) shows the comparison between the normalized growth rate v/v_{lin} (open circles) calculated by VSM and v^c_{lin}/v_{lin} (closed circles) estimated by the compressible linear theory (the values of the sixth row in Table I). The velocities v/v_{lin} in VSM are calculated as the average of bubble and spike velocities at $t = 0$, where we take its absolute value for the bubble velocity. As we see from the figure, both lines v^c_{lin}/v_{lin} and v/v_{lin} are nonlinear with respect to the shock intensity $(p_1 - p_0)/p_1$, and they decrease as the shock intensity increases. Since the bulk vortices in VSM are sizeless, there exists the quantitative difference between v^c_{lin}/v_{lin} and v/v_{lin}; however, the tendency that the strong shock suppresses the growth of RMI is found in both cases.

The cross and the closed square at $(p_1 - p_0)/p_1 = 0.9$ [case (I)] in Fig. 2(b) denote the values of v/v_{lin} that the bulk point vortices in region 2 (the lighter fluid region) and region 1 (the heavier fluid region) are absent, respectively. The value denoted by the closed square largely deviates from the corresponding open circle. On the other hand, the value depicted by the cross almost coincides with the one described by the open circle at the same shock intensity. This indicates that the vortex pair in the heavier fluid (fluid 1) governs the suppression of the growth of the interface and the vortex pair in the lighter fluid (fluid 2) almost do not affect the growth rate of RMI. Therefore, the bulk vortices behind the transmitted shock strongly affect the RMI growth. We mention that when we set stronger vortices than the ones given by Eq. (15) at the same positions y_1 and y_2, the growth rate v/v_{lin} becomes small in comparison to the open circle in Fig. 2(a) at the same shock intensity.

Figure 2(b) denotes the relation between the normalized growth rate v/v_{lin} calculated by VSM and the normalized bulk vorticity ω_1/k in Table I. From this figure, we see that as the bulk vorticity increases, the growth rate decreases, which indicates that increasing bulk vorticity suppresses the growth of RMI. Figure 2(b) quantitatively shows that the bulk vortices, specifically generated behind the transmitted shock, reduce the linear growth rate determined from the initial velocity shear generated at the interface when an incident shock passes

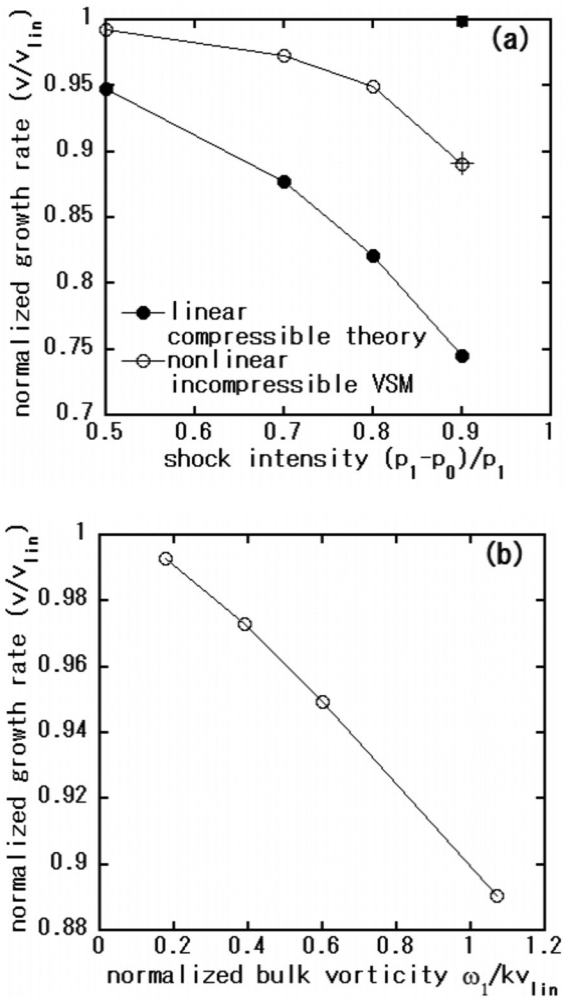

FIG. 2. Vorticity and the linear growth rate: (a) comparison between the normalized growth rate v/v_{lin} calculated by VSM and v^c_{lin}/v_{lin}, and (b) normalized growth rate v/v_{lin} vs normalized vorticity $\omega_1/(kv_{lin})$ [ω_1/k in the normalization in Eq. (15)].

through a corrugated interface. We mention that the reversed trend is observed in later stages, as shown in Figs. 8 and 11.

The reduction of the growth velocity observed in the early stage of the instability becomes small for the spike growth as the increase in the corrugation amplitude with time. We present the evolution of the growth rate of bubble and spike for case (I) in Fig. 3. The solid blue and red lines denote the bubble and spike velocities for RMI with bulk point vortices, and the dotted lines with corresponding colors denote those for RMI without bulk point vortices. The bubble velocities (blue lines) asymptotically tend to zero for both cases with and without bulk point vortices. On the other hand, the growth rate of spike velocity with point vortices (solid red line) increases with time compared to that without bulk point vortices (dotted red line), and both velocities eventually tend to almost the same value at $t = 0.6$. These tendencies for the growth rate of bubble and spike velocities are also found in other shock intensities; however, the difference of two lines in the

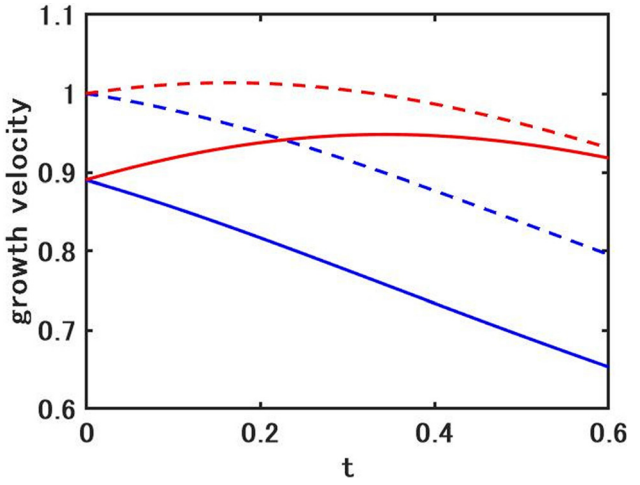

FIG. 3. Temporal evolution of the growth rate of bubble (blue) and spike (red) in case (I) for $\delta = 0$, where the solid lines denote the bubble and spike velocities for RMI with bulk point vortices, and the dotted lines denote those for RMI without bulk point vortices.

growth rate of spike velocities is most notable in the largest shock as case (I). The growth of higher harmonics becomes noticeable at $t \sim 0.2$, and asymmetry for the profile of bubble and spike appears at around this time. In the linear theory, bubbles and spikes have the same growth rate and symmetry; however, in the nonlinear model, bubbles and spikes have different growth rates. Also, even if the corrugation amplitude is about 1/30 of the wavelength, we cannot ignore the higher-order Fourier modes, and the shapes of spikes and bubbles are not symmetric. In the current study, this becomes remarkable at around $t = 0.2$.

Figure 4 shows the interfacial structures and the velocity fields with bulk point vortices for case (I), where the left and right figures show $t = 0$ and $t = 0.6$, respectively. The numerical method to observe the velocity field is found in Refs. 9 and 31. The lower fluid is heavier fluid (fluid 1), and the upper one is lighter fluid (fluid 2). The red and

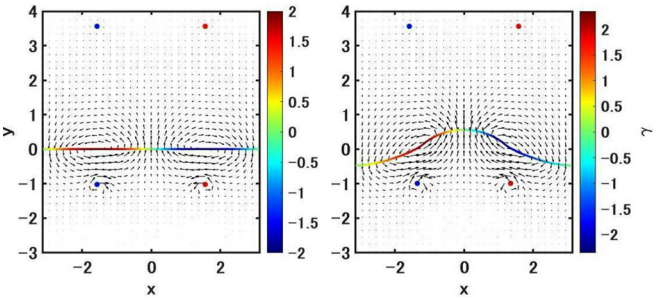

FIG. 4. Interfacial structures for $\delta = 0$ with the colored scale of the vortex sheet strength γ and the velocity fields for case (I), where the left and right figures show $t = 0$ and $t = 0.6$, respectively. The red and blue points denote the point vortices with counterclockwise rotation (positive sign) and clockwise rotation (negative sign), respectively. The initial positions of P_i ($i = 1, 2, 3, 4$) are given by Eq. (15). When $t = 0.6$ (right figure), the positions of point vortices are $P_1 = (1.59, 3.56)$, $P_2 = (1.35, -0.99)$, $P_3 = (-1.59, 3.56)$, and $P_4 = (-1.35, -0.99)$.

blue points in bulk denote the point vortices with counterclockwise rotation (positive sign) and clockwise rotation (negative sign), respectively. The deformation of the flow around the point vortices is clearly seen in Fig. 4. It should be noted that the position of the bulk vortices does move due to the nonlinear interaction with the interface vorticity, unlike the linear theory.[31] The vortices move due to the background flow induced by the sheared interface and self-interaction between the point vortices when their distance becomes shorter. Their trajectory will be shown below in Fig. 10 in detail. The bulk point vortices 1 and 3 in Eq. (15) located in fluid region 2 (upper region) almost do not move up to the state $t = 0.6$. This is because the vortex pair is away from the interface, by which the vortex pair in the lighter fluid interacts very weakly with the vortex sheet, at least up to this time. The bulk point vortices 2 and 4 in Eq. (15) located in fluid region 1 (lower region) eventually approach the interface, and the distance between the two vortices becomes closer. The evolution of the system is almost determined by the interaction between these bulk vortices in region 1 and the interface. The lower region corresponds to the region behind the transmitted shock in RMI.

As the amplitude of the interface corrugation becomes the order of $\lambda/10$ (λ the wavelength), the nonlinear interaction between the bulk vorticity and the interface vorticity becomes very important. We show the interfacial structures with the colored scale of the vortex sheet strength γ with [left; case (I)] and without (right) bulk point vortices at $t = 0.6$ in Fig. 5. Since the bubble and spike velocities in RMI with bulk point vortices are smaller than those in RMI without bulk point vortices (refer to Fig. 3), the amplitudes of bubble and spike in RMI with bulk point vortices become smaller than those in RMI without bulk point vortices at this time. From Figs. 2, 3, and 5, we can conclude that the existence of bulk vortices suppresses RMI, at least in the earlier stage of its evolution.

Figure 6 shows the evolution of the absolute value of the maximum vortex sheet strength $|\gamma|$ in case (I), where the red and blue lines denote the sheet strength for RMI with and without bulk point vortices, respectively. The maximum sheet strength appears in the neighborhood of $x = \pm\pi/2$ [refer to the initial condition Eq. (14) and also see Fig. 7]. As we see from the figure, the maximum vortex sheet strength with bulk point vortices (red line) grows much faster and becomes much larger than that without bulk point vortices (blue line) in the nonlinear stage. From Figs. 2, 3, and 6, we see that although the existence of bulk vortices suppresses the growth of RMI in the early stage, the vortex sheet strength increases.[31]

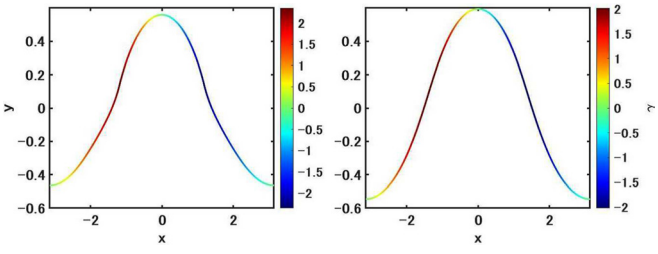

FIG. 5. Interfacial structures for $\delta = 0$ with the colored scale of the vortex sheet strength γ at $t = 0.6$, where the left and right figures show the interface with and without bulk point vortices for case (I).

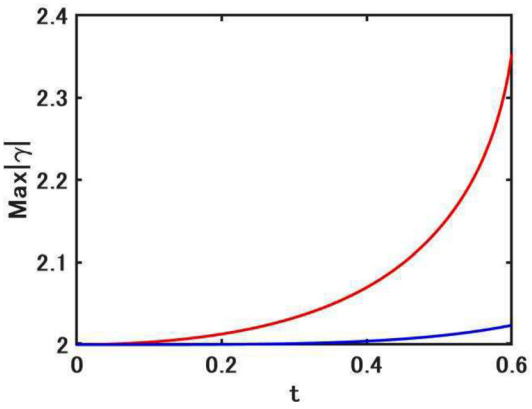

FIG. 6. Temporal evolution of the absolute value of the maximum sheet strength γ in case (I), where the red and blue lines denote the maximum value of $|\gamma|$ on the interface with and without bulk point vortices, respectively.

We depict the corresponding curvature of the interface structure shown in Fig. 5 as a function of the Lagrange parameter e in Fig. 7, where the left and right figures show the curvature of the interface with and without bulk point vortices. Although the interfacial structure of the left figure in Fig. 5 is sufficiently smooth, the corresponding curvature in Fig. 7 has cusps at the vortex cores ($e \sim \pm\pi/2$),[47] at which the vortex sheet strength $|\gamma|$ takes its maximum value. On the other hand, such cusps are not found in the right figure of Fig. 7 at this time yet. This suggests that Moore's curvature singularity[28,45] in RMI with bulk point vortices occurs at an earlier stage than that in RMI without bulk point vortices, which indicates that the suppression of the growth rate of bubble and spike does not necessarily stabilize the evolution of the Kelvin–Helmholtz instability.[42,45] The numerical calculation for $\delta = 0$ with bulk point vortices breaks down immediately after ($t = +0.6$) the appearance of the curvature singularity. We mention that the cusps, as found in the left figure of Fig. 7, appears in the neighborhood of $e = \pm\pi/2$ at $t = 0.93$ for RMI without bulk point vortices, and the calculation breaks down immediately after this time. In the current study, Moore's curvature singularity appears when the corrugation amplitude becomes about 1/10 of the wavelength.

D. Long time nonlinear interfacial dynamics by VSM for $\delta \neq 0$

In this subsection, we present the numerical results by VSM for $\delta \neq 0$. The calculation for $\delta \neq 0$ does not possess the analytical

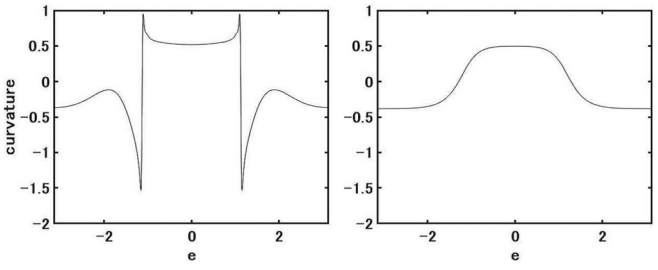

FIG. 7. Curvature of the interfaces at $t = 0.6$, where the left and right figures show the curvature of the interface with and without bulk point vortices.

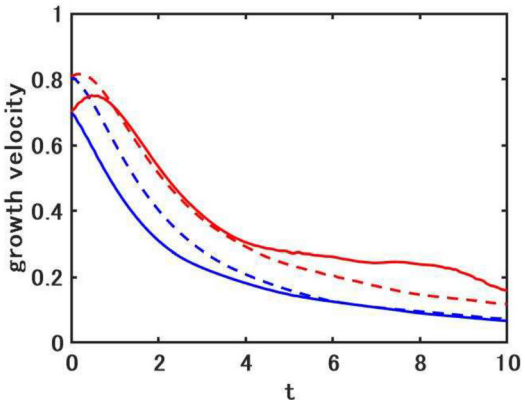

FIG. 8. Temporal evolution of (the absolute value of) the growth rate of bubble and spike for $\delta = 0.15$, where the solid blue and red lines denote the bubble and spike velocities for RMI with bulk point vortices, and the dotted blue and red lines denote those for RMI without bulk point vortices.

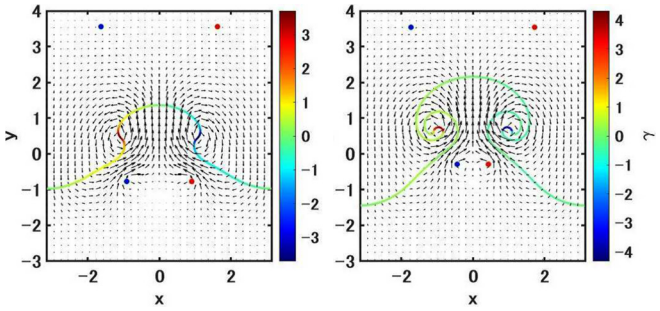

FIG. 9. Interfacial structures for $\delta = 0.15$ with the colored scale of the vortex sheet strength γ and the velocity fields, where the left and right figures show $t = 2$ and $t = 4$, respectively. The colors of point vortices are the same as those in Fig. 4. The initial positions of P_i ($i = 1, 2, 3, 4$) are the same as Fig. 4. In the left figure ($t = 2$), the positions of point vortices are $P_1 = (1.63, 3.56)$, $P_2 = (0.91, -0.77)$, $P_3 = (-1.63, 3.56)$, $P_4 = (-0.91, -0.77)$, and the corresponding positions in the right figure ($t = 4$) are $P_1 = (1.73, 3.54)$, $P_2 = (0.44, -0.29)$, $P_3 = (-1.73, 3.54)$, $P_4 = (-0.44, -0.29)$.

accuracy as for the calculation in $\delta = 0$ presented in Subsec. IV C; however, it enables us to compare the numerical result to the long-time behavior in experiments[59] or hydrodynamic simulations.[9,15] Here, we adopt δ as $\delta = 0.15$. The value $\delta = 0.15$ is best suited for experiments by Jacobs *et al.*[28,59] and the results by the above hydrodynamic simulations. We mention that there is not much of a difference in the results between $\delta = 0.1$ and $\delta = 0.15$.[28] In numerical calculations, the number of grid points N is chosen as $N = 512$, and we set the normalized time step Δt as $\Delta t = 2.5 \times 10^{-3}$ throughout the calculations for $\delta = 0.15$. We consider the case (I) in this subsection.

Figure 8 shows the evolution of the growth rate of bubble and spike for $\delta = 0.15$. The colors and line types are the same as those in Fig. 3. The discrepancy of the initial growth rate between Figs. 3 and 8 is due to the finite value δ. As we see from the figure, the bubble velocities (blue lines) asymptotically tend to zero for both RMI with and without bulk point vortices. The growth velocity of spike also decreases with time for both with and without bulk vortices. However, the growth velocity of spike is more notably affected by bulk point vortices. The growth velocity of spike with bulk point vortices (red solid line) begins to deviate from the one without bulk point vortices (red dotted line) at around $t = 4$, at which the bulk point vortices in region 1 (heavier fluid) approach the interface, and the deformation of spike due to the interaction between bulk vortices and the interface begins. Unlike the case of $\delta = 0$ (Fig. 3), the spike velocity for $\delta = 0.15$ with bulk point vortices is asymptotically larger than that without bulk point vortices (also refer to Fig. 11 below). The growth velocity of bubbles decays with $1/t$ for both cases with and without bulk point vortices.

The increase in the spike growth at around $t = 4$ in Fig. 8 for the case with the bulk vortices can be understood as follows. Due to the background flow in which the point vortices are induced by the vorticity on the interface, the distance between the point vortices in the lower region becomes shorter, and they are carried to the root of the spike, as shown in Fig. 9. These point vortices increase the flow to the tip of the spike, and further to the tip of the mushroom umbrella, as shown in Fig. 11. As a result, the nonlinear growth of the spike is greater than it would be without the point vortex.

We present the interfacial structures for $\delta = 0.15$ and the velocity fields with bulk point vortices at $t = 2$ and $t = 4$ in Fig. 9. As with the case of $\delta = 0$ (Fig. 4), the point vortices in the upper region [point vortices 1 and 3 in Eq. (15)] almost do not move up to this time $t = 4$. On the other hand, the point vortices in the lower region [point vortices 2 and 4 in Eq. (15)] located in the heavier fluid approach the interface and increase the vortex sheet strength γ by interacting with the interface. The distance between the point vortices in the lower heavy region becomes shorter at time $t \sim 4$, mainly due to the background flow induced by the vortex sheet. Owing to this interaction between the non-uniform vortex sheet (interface) and the bulk vortices, the shape of the interface is deformed, and the growth rate of spike deviates from the one without bulk point vortices (refer to Figs. 8 and 11).

The trajectories of point vortices with (left figure) and without (right figure) the interface are depicted in Fig. 10. When the interface is absent, both vortex pairs located in fluid 1 and fluid 2 almost do not move. This indicates that two vortices [point vortices 1 and 3 or point vortices 2 and 4 in Eq. (15)] without the interface cannot form a vortex pair because the distance between them is too far. On the other hand,

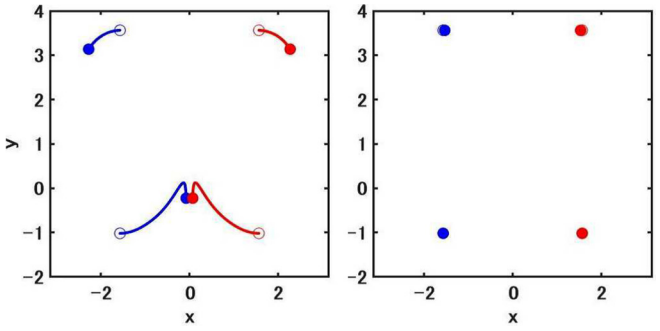

FIG. 10. Trajectories of point vortices (left) with and (right) without the interface for the initial condition (15), where the colors of point vortices are the same as those in Figs. 4 and 9, and both figures take the same period of time ($0 \le t \le 10$). The markers of white circle and filled circle denote the initial and final positions of point vortices, respectively.

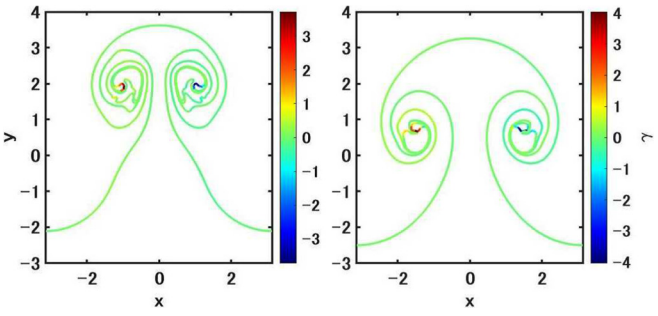

FIG. 11. Interfacial structures for $\delta = 0.15$ with the colored scale of the vortex sheet strength γ at $t = 10$, where the left and right figures show the interface with and without bulk point vortices.

when the interface exists, the background flow induced by the vortex sheet pushes the point vortices closer in the lower region, and then a vortex pair is formed. Since the strength of the vortex pair has the opposite sign, it moves in parallel. The translation direction is downward ($9 < t \leq 10$). This phenomenon that the vortex pair moves downward in parallel against the flow induced by the vortex sheet was not observed in our previous work.[31] In the previous study, the point vortices move up into the spike and mushroom. This difference in the dynamics of point vortices may be due to the weaker vorticity in the previous work compared to case (I). Details of the dynamics of the point vortices for weaker vorticity will be discussed in the future. The vortices in the upper region move outward due to the flow induced by the vortex sheet. Since their vorticity is weak, and they locate far away from the interface compared with ones in the lower region, the vortices in the upper region do not affect much on the dynamics of the interface.

We present the interfacial structures with the colored scale of the vortex sheet strength γ with (left) and without (right) bulk point vortices at the final stage $t = 10$ in Fig. 11. The amplitude of spike in the left figure is larger than the one in the right figure. This can be understood as follows. As observed in Fig. 10, the vortices in the lower region pump up the flow into the spike, which enhances the growth of the spike and the roll-up of the interface. Therefore, the strong vortices in the lower region, i.e., vortices generated behind the transmitted shock, play a different role in the nonlinear evolution in RMI. In the earlier stage, they suppress the growth; however, in the fully nonlinear stage such that the amplitude of the interface corrugation becomes the order of the wavelength, they enhance the spike growth.

V. CONCLUDING REMARKS

We have investigated the linear and nonlinear interaction between the interface and bulk point vortices in RMI using VSM. The initial vorticity of the vortex sheet is determined by the non-uniform velocity shear deposited on the interface when a planar incident shock passes through a corrugated interface, which is calculated from the linear theory. The initial strength and positions of point vortices are determined from the vortices behind the transmitted and the reflected shocks in the compressible linear theory. The result obtained from the compressible linear theory that the existence of bulk vortices suppresses RMI was also confirmed in the incompressible VSM with bulk point vortices, at least in the linear stage. The suppression was evaluated as a function of the bulk vorticity, and it was compared with the linear theory. In the fully nonlinear stage, the bulk vortices significantly affect the interfacial structure and nonlinear growth of the spike. Unlike the suppression observed in the early stage, the bulk vortices enhance the growth of the spike by supplying flow to the spike. In both early and fully nonlinear stages, the bulk vortices in the heavier fluid, i.e., vortices behind the transmitted shock, play important roles. VSM can capture such interfacial deformations and dynamics of bulk point vortices for a long time.

ACKNOWLEDGMENTS

The authors would like to thank Professor J. G. Wouchuk and Dr. T. Sano for their useful comments. This work was supported by Grant-in-Aid for Scientific Research (B) (Grant No. 20H01880) and (C) (Grant Nos. 17K05371 and 18K03418) from the Japan Society for the Promotion of Science, the Osaka City University (OCU) Strategic Research Grant for top priority researches 2019, and the joint research project of ILE, Osaka University. F.C.-C. has received support from MINECO under Grant No. ENE2016–75703-R, from JCCM Grant No. SB-PLY/17/180501/000264, and from a 2019 Leonardo Grant for Researchers and Cultural Creators, BBVA Foundation, awarded to C. Huete.

DATA AVAILABLITY

The data that support the findings of this study are available from the corresponding author upon reasonable request.

REFERENCES

[1]R. D. Richtmyer, "Taylor instability in shock acceleration of compressible fluids," Commun. Pure Appl. Math. **13**, 297–319 (1960).
[2]E. E. Meshkov, "Instability of the interface of two gases accelerated by a shock wave," Fluid Dyn. **4**, 101–108 (1972).
[3]K. Nishihara, J. G. Wouchuk, C. Matsuoka, R. Ishizaki, and V. V. Zhakhovskii, "Richtmyer-Meshkov instability: Theory of linear and nonlinear evolution," Philos. Trans. R. Soc. A **368**, 1769–1807 (2010).
[4]Y. Zhou, "Rayleigh-Taylor and Richtmyer-Meshkov instability induced flow, turbulence, and mixing. I," Phys. Rep. **720–722**, 1–136 (2017).
[5]S. I. Abarzhi, A. K. Bhowmick, A. Naveh, A. Pandian, N. C. Swisher, R. F. Stellingwerf, and W. D. Arnett, "Supernova, nuclear synthesis, fluid instabilities, and interfacial mixing," Proc. Natl. Acad. Sci. U. S. A. **116**, 18184–18192 (2019).
[6]R. Y. T. Inoue and S. Inutsuka, "Turbulence and magnetic field amplification in supernova remnants: Interactions between a strong shock wave and multiphase interstellar medium," Astrophys J. **695**, 825 (2009).
[7]T. Sano, K. Nishihara, C. Matsuoka, and T. Inoue, "Magnetic field amplification associated with the Richtmyer-Meshkov instability," Astrophys. J. **758**, 126 (2012).
[8]T. Sano, T. Inoue, and K. Nishihara, "Critical magnetic field strength for suppression of the Richtmyer-Meshkov instability in plasmas," Phys. Rev. Lett. **111**, 205001 (2013).
[9]C. Matsuoka, K. Nishihara, and T. Sano, "Nonlinear dynamics of non-uniform current-vortex sheets in magnetohydrodynamic flows," J. Nonlinear Sci. **27**, 531–572 (2017).
[10]G. Dimonte, C. E. Frerking, M. Schneider, and B. Remington, "Richtmyer-Meshkov instability with strong radiatively driven shocks," Phys. Plasmas **3**, 614–630 (1996).
[11]J. Lindl, *Inertia Confinement Fusion: The Quest for Ignition and High Gain Using Indirect Drive* (Springer/AIP, New York, 1997).
[12]R. L. Holmes, G. Dimonte, B. Fryxell, M. L. Gittings, J. W. W. Grove, H. Schneider, D. Sharp, A. L. Velikovich, R. Weaver, and Q. Zang, "Richtmyer-

Meshkov instability growth: Experiment, simulation and theory," J. Fluid Mech. **389**, 55–79 (1999).
[13]A. L. Velikovich, J. G. Wouchuk, C. H. R. de Lira, N. Melzler, S. Zalesak, and A. J. Schmitt, "Shock front distortion and Richtmyer-Meshkov-type growth caused by a small preshock nonuniformity," Phys. Plasmas **14**, 072706 (2007).
[14]J. G. Wouchuk and K. Nishihara, "Asymptotic growth in the linear Richtmyer-Meshkov instability," Phys. Plasmas **4**, 1028–1038 (1997).
[15]C. Matsuoka, K. Nishihara, and Y. Fukuda, "Nonlinear evolution of an interface in the Richtmyer-Meshkov instability," Phys. Rev. E **68**, 036301 (2003).
[16]J. G. Wouchuk, C. H. R. de Lira, and A. L. Velikovich, "Analytical linear theory for the interaction of a planar shock wave with an isotropic turbulent vorticity field," Phys. Rev. E. **79**, 066315 (2009).
[17]F. Cobos-Campos and J. G. Wouchuk, "Analytic solution for the zero-order postshock profiles when an incident planar shock hits a planar contact surface," Phys. Rev. E **100**, 033107 (2019).
[18]J. G. Wouchuk, "Growth rate of the linear Richtmyer-Meshkov instability when a shock is reflected," Phys. Rev. E **63**, 056303 (2001).
[19]G. Fraley, "Rayleigh-Taylor stability for a normal shock wave-density discontinuity interaction," Phys. Fluids **29**, 376–386 (1986).
[20]M. Stanic, R. F. Stellingwerf, J. T. Cassibry, and S. I. Abarzhi, "Scale coupling in Richtmyer-Meshkov flows induced by strong shocks," Phys. Plasmas **19**, 082706 (2012).
[21]M. Stanic, R. F. Stellingwerf, J. T. Cassibry, and S. I. Abarzhi, "Non-uniform volumetric structures in Richtmyer-Meshkov flows," Phys. Fluids **25**, 106107 (2013).
[22]M. Vandenboomgaerde, D. Souffland, C. Mariani, L. Biamino, G. Jourdan, and L. Houas, "An experimental and numerical investigation of the dependency on the initial conditions of the Richtmyer-Meshkov instability," Phys. Fluids **26**, 024109 (2014).
[23]Z. Dell, R. F. Stellingwerf, and S. I. Abarzhi, "Effect of initial perturbation amplitude on Richtmyer-Meshkov flows induced by strong shocks," Phys. Plasmas **22**, 092711 (2015).
[24]F. Cobos-Campos and J. G. Wouchuk, "Analytical scalings of the linear Richtmyer-Meshkov instability when a shock is reflected," Phys. Rev. E **93**, 053111 (2016).
[25]J. G. Wouchuk and K. Nishihara, "Linear perturbation growth at a shocked interface," Phys. Plasmas **3**, 3761–3776 (1996).
[26]F. Cobos-Campos and J. G. Wouchuk, "Analytical scalings of the linear Richtmyer-Meshkov instability when a rarefaction is reflected," Phys. Rev. E **96**, 013102 (2017).
[27]H. Lamb, *Hydrodynamics* (Dover, New York, 1932).
[28]C. Matsuoka and K. Nishihara, "Vortex core dynamics and singularity formations in incompressible Richtmyer-Meshkov instability," Phys. Rev. E **73**, 026304 (2006).
[29]C. Matsuoka and K. Nishihara, "Fully nonlinear evolution of a cylindrical vortex sheet in incompressible Richtmyer-Meshkov instability," Phys. Rev. E **73**, 055304(R) (2006).
[30]C. Matsuoka and K. Nishihara, "Analytical and numerical study on a vortex sheet in incompressible Richtmyer-Meshkov instability in cylindrical geometry," Phys. Rev. E **74**, 066303 (2006).
[31]C. Matsuoka and K. Nishihara, "Nonlinear interaction between bulk point vortices and an unstable interface with non-uniform velocity shear such as Richtmyer-Meshkov instability," Phys. Plasmas **27**, 052305 (2020).
[32]R. Krasny, "A study of singularity formation in a vortex sheet by the point vortex approximation," J. Fluid Mech. **167**, 65–93 (1986).
[33]R. Krasny, "Computation of vortex sheet roll-up in the Trefftz plane," J. Fluid Mech. **184**, 123–155 (1987).
[34]G. Baker, D. I. Meiron, and S. A. Orszag, "Generalized vortex methods for free surface flow problems," J. Fluid Mech. **123**, 477–501 (1982).
[35]S.-I. Sohn, D. Yoon, and W. Hwang, "Long-time simulations of the Kelvin-Helmholtz instability using an adaptive vortex method," Phys. Rev. E **82**, 046711 (2010).
[36]S.-I. Sohn, "Late-time vortex dynamics of Rayleigh-Taylor instability," J. Phys. Soc. Jpn. **80**, 084401 (2011).
[37]C. Matsuoka, "Vortex sheet motion in incompressible Richtmyer-Meshkov and Rayleigh-Taylor instabilities with surface tension," Phys. Fluids **21**, 092107 (2009).
[38]C. Matsuoka, K. Nishihara, and T. Sano, "Nonlinear interfacial motion in magnetohydrodynamic flows," High Energy Density Phys. **31**, 19–23 (2019).
[39]G.-H. Cottet and P. D. Koumoutsakos, *Vortex Methods: Theory and Practice* (Cambridge University Press, Cambridge, 2000).
[40]G. Birkhoff, "Helmholtz and Taylor instability," Proc. Symp. Appl. Math. Soc. **13**, 55–76 (1962).
[41]N. Rott, "Diffraction of a weak shock with vortex generation," J. Fluid Mech. **1**, 111–128 (1956).
[42]P. G. Saffman, *Vortex Dynamics* (Cambridge University Press, Cambridge, 1992).
[43]M. J. Shelley, "A study of singularity formation in vortex-sheet motion by a spectrally accurate vortex method," J. Fluid Mech. **244**, 493–526 (1992).
[44]C. Matsuoka, "Renormalization group approach to interfacial motion in incompressible Richtmyer-Meshkov instability," Phys. Rev. E **82**, 036320 (2010).
[45]D. W. Moore, "The spontaneous appearance of a singularity in the shape of an evolving vortex sheet," Proc. R. Soc. A **365**, 105–119 (1979).
[46]A. L. Velikovich, "Analytic theory of Richtmyer-Meshkov instability for the case of reflected rarefaction wave," Phys. Fluids **8**, 1666–1679 (1996).
[47]N. Zabusky, "Vortex paradigm for accelerated inhomogeneous flows: Visiometrics for the Rayleigh-Taylor and Richtmyer-Meshkov environments," Annu. Rev. Fluid Mech. **31**, 495–536 (1999).
[48]A. L. Velikovich, J. P. Dahlburg, A. J. Schmitt, J. H. Gardner, and L. Phillips, "Richtmyer-Meshkov-like instabilities and early-time perturbation growth in laser targets and z-pinch loads," Phys. Plasmas **7**, 1662–1671 (2000).
[49]Y. Yang, Q. Zhang, and D. H. Sharp, "Small amplitude theory of Richtmyer-Meshkov instability," Phys. Fluids **6**, 1856–1873 (1994).
[50]P. K. Newton, *The N-Vortex Problem* (Springer, New York, 2000).
[51]D. I. Pullin, "Numerical studies of surface-tension effects in nonlinear Kelvin-Helmholtz and Rayleigh-Taylor instability," J. Fluid Mech. **119**, 507–532 (1982).
[52]R. M. Kerr, "Simulation of Rayleigh-Taylor flows using vortex blobs," J. Comput. Phys. **76**, 48–84 (1988).
[53]J. G. Wouchuk, "Growth rate of the Richtmyer-Meshkov instability when a rarefaction is reflected," Phys. Plasmas **8**, 2890–2907 (2001).
[54]J. G. Wouchuk and F. Cobos-Campos, "Kinetic energy of the rotational flow behind an isolated rippled shock wave," Phys. Scr. **93**, 094003 (2018).
[55]A. Sidi and M. Israeli, "Quadrature methods for periodic singular and weakly singular Fredholm integral equations," J. Sci. Comput. **3**, 201–231 (1988).
[56]G. Baker and A. Nachbin, "Stable methods for vortex sheet motion in the presence of surface tension," SIAM J. Sci. Comput. **19**, 1737–1766 (1998).
[57]S. I. Abarzhi, K. Nishihara, and J. Glimm, "Rayleigh-Taylor and Richtmyer-Meshkov instabilities for fluids with a finite density ratio," Phys. Lett. A **317**, 470–476 (2003).
[58]M. Herrmann, P. Moin, and S. Abarzhi, "Nonlinear evolution of the Richtmyer-Meshkov instability," J. Fluid Mech. **612**, 311–338 (2008).
[59]J. W. Jacobs and J. M. Sheeley, "Experimental study of incompressible Richtmyer-Meshkov instability," Phys. Fluids **8**, 405–415 (1996).